NeuroImage 202 (2019) 116121

Contents lists available at ScienceDirect

NeuroImage

journal homepage: www.elsevier.com/locate/neuroimage

Tractography delineation of the vertical occipital fasciculus using quantitative T1 mapping

Roey Schurr *, Shir Filo, Aviv A. Mezer

Edmond & Lily Safra Center for Brain Sciences, The Hebrew University of Jerusalem, Jerusalem, Israel

A B S T R A C T

The vertical occipital fasciculus (VOF) is a white-matter tract that connects the ventral and dorsal visual streams. The precise borders of the VOF have been a matter of dispute since its discovery in the 19th century. The presence of an adjacent vertical pathway, the posterior arcuate fasciculus, makes it especially hard to determine the anterior extent of the VOF. By integrating diffusion MRI tractography with quantitative T1 mapping we found that the vertical streamlines originating in the ventral occipito-temporal cortex show a pattern of lower T1 in more posterior streamlines. We used this pattern to develop an automatic procedure for VOF identification based on a sharp increase in the streamline T1 signature along the posterior-anterior axis. We studied the cortical endpoints of the VOF and their relation to known cytoarchitectonic and functional divisions of the cortex. These results show that multi-modal MRI information, which characterizes local tissue microstructure such as myelination, can be used to delineate white-matter tracts *in vivo*.

1. Introduction

The vertical occipital fasciculus (VOF) is a white-matter tract connecting ventral and dorsal regions in the occipital, temporal and parietal lobes. Decades after it was first described, the VOF was only recently rediscovered, drawing great attention from the scientific community (Briggs et al., 2018; Takemura et al., 2016; Weiner et al., 2016; Yeatman et al., 2014b). The precise location of the VOF, and in fact its very existence, has been a matter of dispute since it was first described by Wernicke (Yeatman et al., 2014b). One of the factors contributing to this dispute is the existence of the adjacent posterior arcuate fasciculus (pAF), another vertical white-matter tract, just anterior to the VOF (Curran, 1909; Weiner et al., 2016) (Fig. 1).

In vivo identification of the VOF is important for the study of visual cognitive function in the healthy population, as well as its disruption in diseased populations (Budisavljevic et al., 2018; Duan et al., 2015; Lee Masson et al., 2017; Oishi et al., 2018). The pAF, which connects ventral and dorsal regions involved in language processing, is important for the study of uniquely human language functions (Catani et al., 2005; Weiner et al., 2016). Several recent works have identified the VOF *in vivo*, although a definitive definition of its exact location, especially with regards to its anterior extent, is still missing (Briggs et al., 2018; Keser et al., 2016; Takemura et al., 2017; Wang et al., 2016; Weiner et al., 2016). In some axial diffusion MRI slices, two clusters of vertically oriented fibers are visible, presumably belonging to the VOF and pAF. These clusters are often separated by the ascending branch of the superior temporal sulcus (STS) and by the anterior occipital sulcus (AOS) on lower slices (Takemura et al., 2017). Individual variability in tractography results is known to exist in this region: in some subjects, the vertical streamlines comprise of two fully separated bundles, while in others, they form a continuous sheet (Weiner et al., 2016). Hence, the geometry of these tracts often precludes the identification of the border between them.

Different approaches exist for delineating specific white-matter tracts using diffusion MRI tractography. These approaches rely on recognizing a unique property that distinguishes the tract-relevant streamlines from all others. Most commonly, tract-specific streamlines are identified based on spatial criteria, such as passing through specific waypoint regions of interest, ending in specific cortical or subcortical regions, or presenting geometrical similarity to some atlas-defined tract (see Wasserthal et al., 2018). Yet white-matter tracts differ not only in their spatial course, but also in their microstructural signatures. For example, different myelin content allows the identification of white-matter tracts post mortem in myelin staining studies (Bürgel et al., 2006). *In vivo*, these distinct microstructural signatures are captured using quantitative MRI parameters, such as quantitative T1 (Schurr et al., 2018; Takemura et al., 2018; Yeatman et al., 2014a), which is sensitive to myelin content (Lutti et al., 2014; Stüber et al., 2014). We have shown previously that T1 provides significant contrast between different white-matter tracts, and can be used to improve the accuracy of *in vivo* tractography of the optic radiation (Schurr et al., 2018). It is still an open question whether other white-matter tracts can be identified using T1 mapping. Here we tested

* Corresponding author.
E-mail address: roey.schurr@mail.huji.ac.il (R. Schurr).

https://doi.org/10.1016/j.neuroimage.2019.116121
Received 18 February 2019; Received in revised form 12 July 2019; Accepted 22 August 2019
Available online 28 August 2019

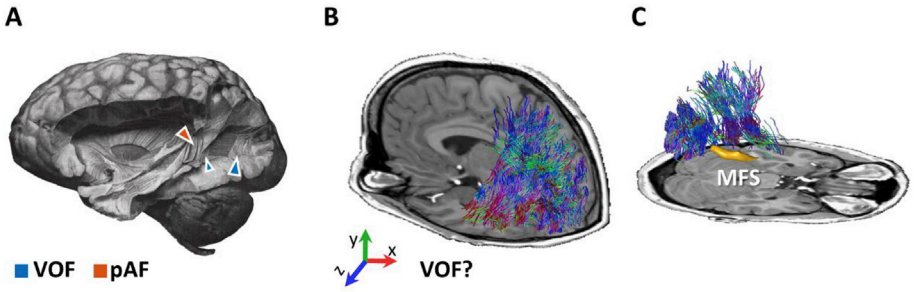

Fig. 1. (A) A post mortem dissected brain showing the VOF (blue) and the pAF (orange), reproduced from Curran (1909). The middle part of the VOF was removed to reveal the sagittal stratum. **(B)** In vivo reconstruction of vertical fascicles originating in the ventral occipito-temporal cortex. These candidate streamlines, colored by orientation, include both the VOF and the pAF. **(C)** The reconstructed vertical streamlines shown from a medial point of view. In this subject, two separate clusters of streamlines can be distinguished. The posterior cluster ends in close proximity to the posterior end of the mid-fusiform sulcus (MFS; yellow). See additional subjects in Supplementary Fig. 2.

whether VOF identification can be facilitated using T1 mapping.

A recent study characterized two sub-regions in the ventral occipito-temporal cortex (vOTC): a posterior region from which the VOF originates and an anterior region from which the pAF originates (Lerma-Usabiaga et al., 2018). These two cortical sub-regions have distinct quantitative T1 signatures, with the posterior region presenting lower T1 values. However, it is unknown whether the tracts originating from these sub-regions, VOF and pAF, also display distinct microstructural signatures. Here we tested whether the VOF can be identified based on its microstructural signature, as reflected by quantitative T1 mapping. We developed an automatic algorithm for identifying the VOF, based on a sharp increase in the streamlines T1 signature along the posterior-anterior axis. We term the resulting posterior tract VOF-T1. We compared the resulting bundle to the results of two published methods for VOF identification, based on spatial and anatomical criteria. We showed that the proposed algorithm is reliable and robust to instrumental biases. Then, we studied how the microstructural signatures of VOF-T1 change across the lifespan. Finally, we characterized the cortical endpoints of VOF-T1 with respect to known cytoarchitectonic and functional atlases.

2. Methods

2.1. Subjects

We used the dataset from Yeatman et al. (2014a) collected at Stanford University. Of the original 102 subjects, we included only subjects with high angular resolution diffusion data (HARDI) and excluded one subject in which the diffusion data did not include the entire vOTC. This yielded a cohort of 89 subjects (41 male; mean + STD age 33 ± 24, range: 7–85 years old). Four additional subjects (3 male, mean + STD age 25 ± 1, range 23–26 years old) were taken from a separate dataset collected at Stanford University (Gomez et al., 2017) and used to test for scan-rescan reliability. In these four subjects, the data required for T1 mapping were acquired a year apart, and the diffusion MRI data several months apart.

Data collection procedures were approved by the Stanford University Institutional Review Board. Healthy subjects were recruited from the San Francisco area and screened to have no neurological, cognitive or psychiatric disorders. Each adult subject provided a written informed consent, and each child provided assent with the consent of their parent or guardian.

In addition, we used a second independent dataset, scanned at the Hebrew University of Jerusalem (HUJI dataset; Filo et al., 2019). We used this dataset to replicate the results of the main dataset, and to test whether the transverse relaxation time, T2, can also be used for VOF identification. Subjects (n = 13; 7 male; mean ± STD 27 ± 3 years old) were screened to have no neurological, cognitive or psychiatric disorders. The experimental procedure was approved by the Helsinki Ethics Committee of Hadassah Hospital, Jerusalem, Israel. Each subject provided written informed consent.

2.2. MRI acquisition and processing

For the main dataset, data were collected at Stanford University's Center for Cognitive and Neurobiological Imaging (www.cni.stanford.edu), using a 3T General Electric Discovery 750 (General Electric Healthcare, Milwaukee, WI, USA) equipped with a 32-channel head coil (Nova Medical, Wilmington, MA, USA).

For the HUJI dataset, data were collected at the ELSC neuroimaging unit at the Hebrew University of Jerusalem, Israel, using a 3T Siemens MAGNETOM Skyra scanner equipped with a 32-channel head receive-only coil.

2.3. T1 mapping

For the main dataset, the longitudinal relaxation time T1 was computed from spoiled gradient (SPGR) echo images acquired at four flip angles (α = 4°, 10°, 20°, 30°, TR = 14 ms, TE = 2.4 ms) with a spatial resolution of 1 mm^3 isotropic. In addition, spin-echo inversion-recovery (SEIR) scans that are free from transmit-coil inhomogeneity were used as described below. The SEIR was scanned with an echo-planar imaging (EPI) readout, a slab inversion pulse, and spectral-spatial fat suppression, with TR = 3 s, echo time set to minimum full, and inversion times of 50, 400, 1200, and 2400 ms. The SEIR resolution was 2 mm^2 in-plane with a slice thickness of 4 mm. To minimize spatial distortions, the EPI readout was performed using an acceleration factor of 2. Whole-brain T1 maps were computed as described previously (Berman et al., 2018; Mezer et al., 2016, 2013). In short, SPGR images are automatically transformed to the conventional AC-PC aligned space, and subsequently used to calculate T1 maps of high resolution, which are biased by B1 excite inhomogeneity. SEIR images are used to calculate low-resolution T1 maps, which are unbiased (Barral et al., 2010). By comparing the two maps and assuming a smooth bias field, one uses the unbiased SEIR data to correct the high-resolution T1 map (for details see Mezer et al. (2016, 2013)). Voxels in which the B1+ bias field was extrapolated and not calculated directly or interpolated were excluded from further analysis. For each subject, we also synthesized a T1-weighted image from the multi flip-angle SPGR images. The analysis pipeline for producing the unbiased T1 maps is an open-source MATLAB code available at (https://github.com/mezera/mrQ). We used Advanced Normalization Tools (ANTs; Avants et al. (2009); https://github.com/ANTsX/ANTs) to non-linearly warp (but not downsample) the T1 map to the space of the diffusion MRI data in each subject. For an analysis of the effect of registration direction (T1 to diffusion MRI or vice versa), see Appendix B.

For the HUJI dataset, we used a similar protocol, with the following changes. The SPGR images were scanned with TR = 19 m and five equally spaced echoes (TE = 3.34–14.02 ms), of which only the first was used for T1 mapping. The SEIR images were acquired with TR = 2920 ms and TE = 49 ms, with a spatial resolution of 2 mm^2 in-plane and a slice thickness of 3 mm.

2.4. Diffusion weighted imaging

For the main dataset, whole-brain diffusion-weighted MRI data were acquired using dual spin-echo diffusion-weighted sequences. Diffusion-weighting gradients were applied at 96 non-collinear directions across the surface of a sphere as determined by the electrostatic repulsion algorithm (Jones et al., 1999). Data were acquired at a spatial resolution of $2\,mm^3$ isotropic, with the strength of the diffusion weighting set to $b = 2000\ s/mm^2$ (TE/TR = 93.60/7800 ms, G = 53 mT/ms, $\delta = 21$ ms, $\Delta = 25.4$ ms). Eight non-diffusion-weighted images ($b = 0$) were scanned at the beginning of each measurement. Subject motion was corrected using a rigid-body alignment, and diffusion gradients were adjusted accordingly. This dual spin-echo sequence does not require eddy current correction because it has a relatively long delay between the RF excitation pulse and image acquisition, which allows sufficient time for the eddy currents to dephase. The diffusion-weighted images were rigidly transformed to match the orientation of the anatomical T1 map, rendering them in the conventional AC-PC aligned space. Tensor-based parameter maps of mean diffusivity (MD) and fractional anisotropy (FA) were calculated for each subject. Preprocessing was implemented in MATLAB (MathWorks, Natwick, MI, USA) and is publicly available as part of the Vistasoft git repository (https://github.com/vistalab/vistasoft/tree/master/mrDiffusion; see dtiInit.m).

For the HUJI dataset, we used a similar protocol, with the following changes. The spatial resolution was $1.5\,mm^3$ isotropic. Diffusion weighting gradients were applied at 64 directions (TE/TR = 95.80/6000 ms, G = 45 mT/ms, $\delta = 32.25$ ms, $\Delta = 52.02$ ms). Eight non-diffusion-weighted images ($b = 0$) were interspersed between the diffusion weighted volumes. In addition, data included non-diffusion-weighted images with reversed phase-encode blips; these were used to correct for susceptibility and eddy current induced distortions using the topup command of the FDT toolbox in FSL (Smith et al., 2004), as described previously (Andersson and Sotiropoulos, 2016; Sotiropoulos et al., 2013).

Since the corrected data is free of EPI-related distortion, we aligned it to the imaging space of the T1 map using FSL's FLIRT affine registration (Jenkinson et al., 2002; Jenkinson and Smith, 2001), rather than using a nonlinear warp, as in the main dataset.

2.5. T2 mapping

For the HUJI dataset, we also collected T2 data. Multi-spin-echo images were acquired, with 10 equally spaced spin echoes of 12–120 ms. The TR was 4210 ms. The scan resolution was 2 mm isotropic. Whole-brain T2 maps were computed using the echo-modulation curve algorithm (Ben-Eliezer et al., 2015). The T2 map was aligned to the imaging space of the diffusion data using FSL's FLIRT rigid-body alignment.

2.6. Spatially-based identification of the VOF

We compared the proposed T1-based procedure with previously published methods for VOF identification. To minimize age contribution, we chose all young adults from our main dataset (age 18–55 years old; n = 32). For each subject, we identified the VOF using two automatic methods based on spatial criteria that require no manual intervention:

1. VOF-anatomy (Weiner et al., 2016; Yeatman et al., 2012). This method is based on minimizing the overlap between VOF and arcuate fasciculus. In short, the vertical streamlines originating at the vOTC are identified, and streamlines that overlap with the pAF or extend anterior to the pAF core are removed.
2. VOF-waypoint (Takemura et al., 2016). This method is based on two axial waypoint regions of interest (ROIs). In short, tractography is restricted to the occipital lobe, and VOF is identified as streamlines passing through both ROIs. Streamlines that are outliers in terms of their direction, length and position are removed. To implement the VOF-waypoint method, we used the publicly available ROIs that the authors supply, and registered them to each of our subjects using FSL's FNIRT.

We note that while the original works by Takemura et al. and Yeatman et al. used LiFE (Caiafa and Pestilli, 2017) to filter the candidate tractogram, here we did not employ such preliminary filtering. On our data, LiFE resulted in sparse VOF streamlines, possibly due to the lower resolution of the diffusion MRI data (see Caiafa and Pestilli (2017) for relevant discussion).

We used the method of Weiner et al. (2016) to automatically identify the pAF using white-matter waypoint ROIs.

2.7. The distinct T1 signatures of the VOF and pAF

To estimate the T1 signatures of the VOF and pAF, we performed several analyses. First, we used AFQ (Yeatman et al., 2012) to calculate the T1 profile along each tract (VOF-anatomy, VOF-waypoint and pAF). Briefly, each streamline was resampled to 100 equally spaced nodes, and the T1 of each node was sampled from the warped T1 map. The tract core was calculated as the robust mean coordinate of all streamlines per node. The T1 tract profile was calculated along the core of the tract as a weighted sum of the T1 values of all the streamlines at any given node, weighted by the Mahalanobis distance from the core of the tract. Second, we calculated the median T1 value along each tract, and calculated the difference between the median T1 of the pAF and each of the VOF tracts within hemisphere.

To test whether the median T1 in pAF is greater than that of the VOF, we performed a one-tailed paired samples Wilcoxon test for each VOF identification method. Finally, we repeated this analysis for VOF-T1.

2.8. T1-based identification of the VOF

The main steps of the proposed procedure are described in this section, and a schematic overview of the steps is given in Fig. 2. We computed a probabilistic whole-brain tractogram of 500,000 streamlines per subject using anatomically-constrained tractography (ACT) with the default tracking parameters as implemented in MRTrix 3.0 (Smith et al., 2012; Tournier et al., 2012). We used the T1-weighted image that was warped to diffusion space to create a gray-matter–white-matter interface image that served as a seeding mask, using the MRtrix function 5tt2gmwmi. From this whole-brain tractogram we extracted the candidate set of vertical streamlines originating from the ventral occipital temporal cortex as implemented in the Automated Fiber Quantification toolbox (AFQ; Weiner et al., 2016; Yeatman et al., 2012). We additionally excluded all streamlines not terminating within 2 mm from the cortex, as identified by FreeSurfer and warped to diffusion space using ANTs.

The median T1 (T1-Mdn) along each streamline was computed using AFQ as in Yeatman et al. (2014a), based on the T1 map that was warped to diffusion space. The first and last six nodes of each streamline were excluded from this analysis to minimize partial volume effects with the cortex (Oishi et al., 2018). To minimize the effects of inaccuracies in B1+ field estimation, any streamline that passed through voxels of extrapolated B1+ for more than 20% of its length was excluded from this part of the analysis. We used the streamlines' T1-Mdn values to identify the anterior border of the VOF as follows:

Candidate streamlines were divided into approximately 60 equally spaced subsets with 75% overlap along the posterior-anterior direction, based on each streamline's median coordinate along this axis (y-Mdn; Fig. 4B, black lines). Any subset with less than 35 streamlines was merged with the subset immediately anterior to it (for example, Fig. 4B, rightmost black line). For each subset, we calculated the median value of the T1-Mdn. We identified the mid-fusiform sulcus (MFS) of each subject bilaterally using FreeSurfer (Fischl, 2012) as described in Weiner et al. (2018), and warped it to the diffusion space using ANTs. To define the anterior border of the VOF we identified the two greatest increases in T1

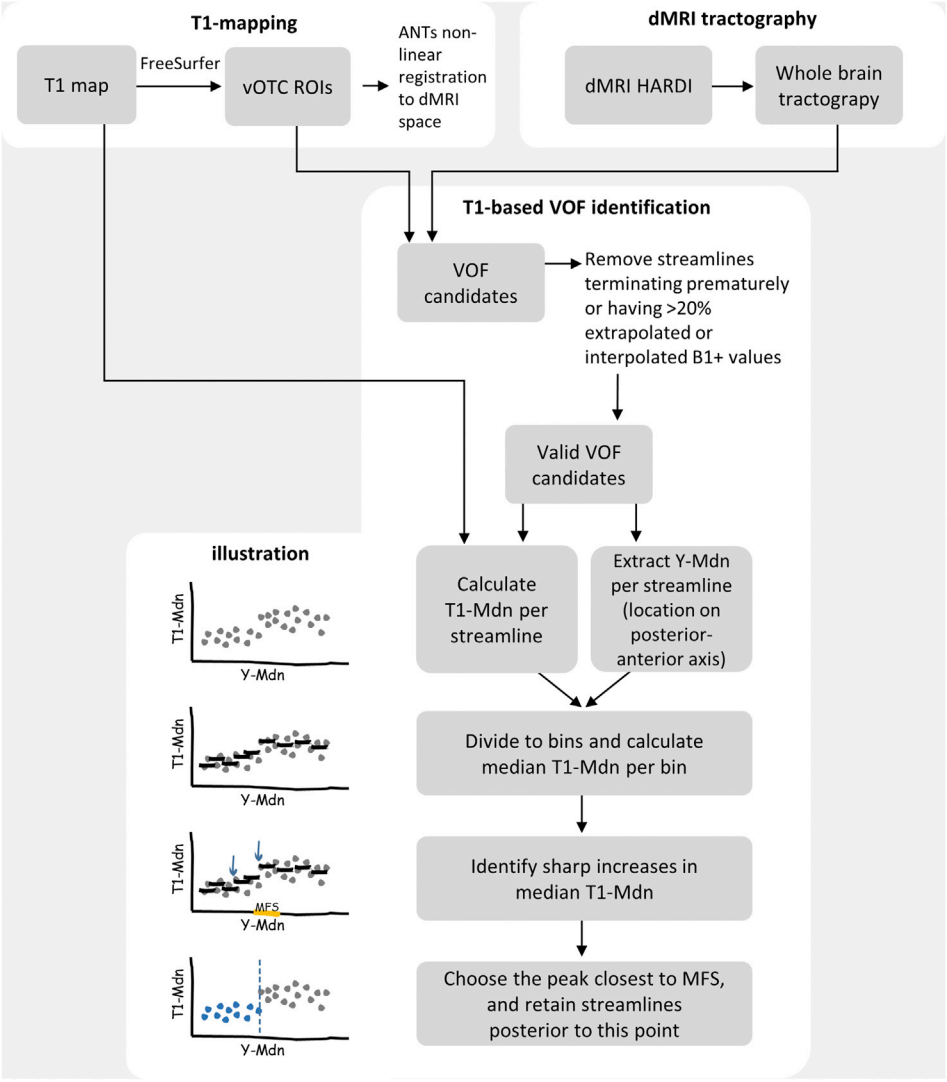

Fig. 2. Summary of the main analysis steps.

between consecutive subsets, and selected the one that resulted in a bundle that terminates closest to the posterior end of the MFS. Any streamline posterior of this point was considered part of VOF-T1.

2.9. Scan-rescan reliability

To assess the reliability of the T1-based identification of the VOF we repeated the analysis for four subjects who were scanned twice with the full protocol.

2.10. Controlling for instrumental biases

A possible concern regarding the T1-based identification procedure is that the increase in T1 values along the posterior-anterior axis does not reflect true properties of the underlying tissue, but rather stems from residual instrumental bias, such as a gradient of B1+ excite field inhomogeneity. To account for this alternative explanation we scanned one subject for T1 mapping at three different head positions within the scanner – once with normal head position, and twice with the head tilted at different angles. Different head positions lead to a different spatial distribution of B1+ inhomogeneity (Bammer et al., 2011). We then repeated the T1-based identification of the VOF using the same candidate streamlines, each time with a different T1 map.

2.11. Comparison with other VOF delineation methods

To quantify the spatial agreement between the VOF-T1 and each spatially-defined VOF, we calculated the Dice coefficient between the voxels traversed by each tract (Dice, 1945):

$$Dice\ Coefficient = \frac{2|A \cap B|}{|A| + |B|}$$

where A are the voxels traversed by one tract and B are the voxels traversed by another tract. The Dice coefficient ranges between 0 (no overlap) and 1 (complete overlap).

In addition, we used the virtual lesion approach (Caiafa and Pestilli, 2017; Pestilli et al., 2014) to estimate the strength of evidence supporting the existence of the VOF, as identified by the different methods. In short, the whole-brain tractogram is used to predict the diffusion signal using the linear fascicle evaluation (LiFE) framework (Pestilli et al., 2014). The strength of evidence S is calculated by removing the streamlines of interest and comparing the root mean squared prediction error of the lesioned and nonlesioned tractograms.

Finally, we calculated the percentage of pAF voxels which are also

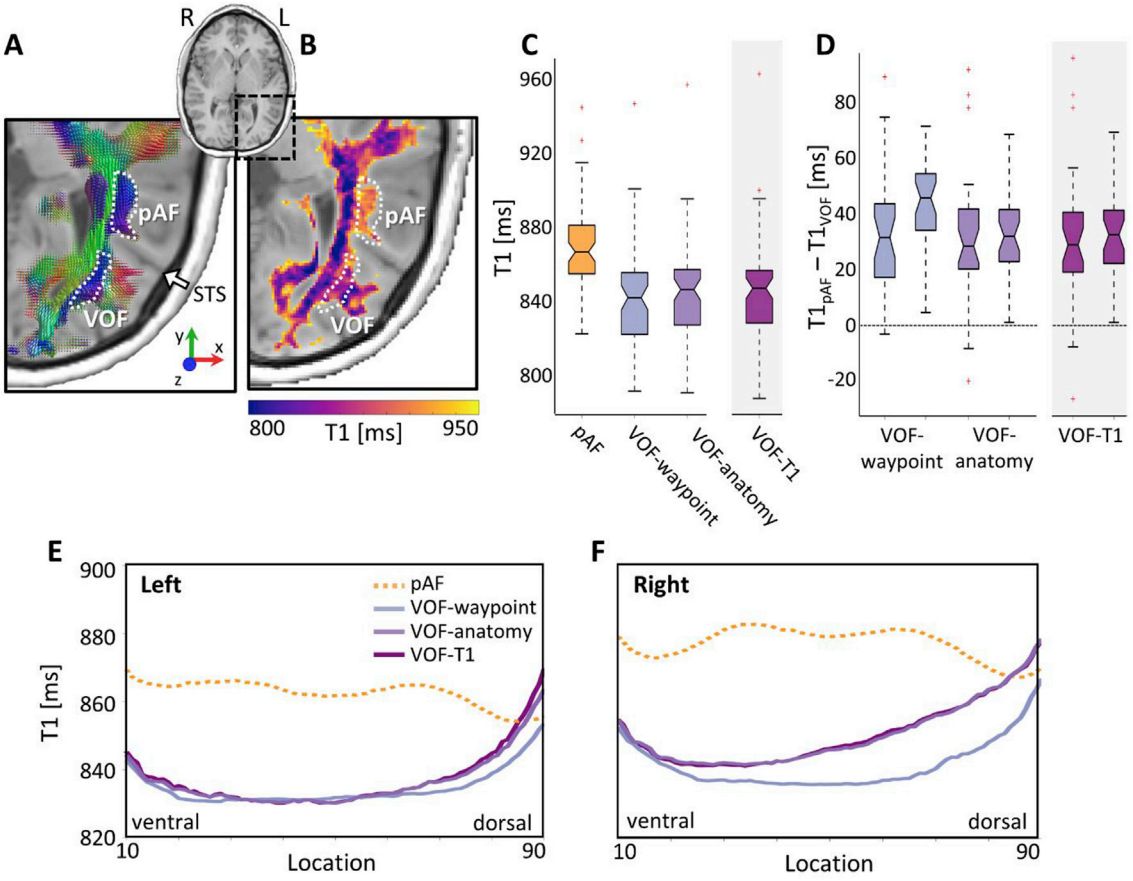

Fig. 3. Microstructural and macrostructural observations of the VOF and pAF. (A) An axial slice of the left hemisphere in one subject, showing the fiber orientation distribution function (colored by orientation) in the white matter overlaid on top of a T1-weighted image. Voxels with vertically oriented fascicles (blue) are apparent where the VOF and pAF are expected, just lateral to the optic radiation (green). In this slice the two clusters are separated by the superior temporal sulcus (STS; white arrow). **(B)** The same voxels in a quantitative T1 map. The more posterior cluster is characterized by lower T1 values. **(C)** Boxplots indicate the distribution of mean T1 values across hemispheres. The VOF shows consistently lower T1 distributions compared with the pAF, for all VOF identification methods. Center lines indicate median values; notch indicates 95% confidence interval for the median; box limits indicate the interquartile range (IQR; 25th-75th percentiles); whiskers extend to the most extreme data points within 1.5 x IQR outside the box. Cases outside this range are individually represented as red crosses. **(D)** Boxplots indicate the within-hemisphere difference between the median T1 in the pAF and the VOF as identified by each method. As expected, this difference tends to be greater than zero. Boxplot location match hemisphere (left and right) **(E-F)** The T1 profile of the VOF and pAF across the population (n = 32 subjects), progressing for ventral to dorsal (10–90), for the left (E) and right (F) hemispheres. The mean profile for each tract is marked with a different color.

traversed by VOF-T1.

2.12. Cortical endpoints of the VOF

For each subject (n = 89), in each hemisphere, the streamlines' endpoints of VOF-T1 were projected onto the cortical gray matter using a 3D Gaussian smoothing kernel (5 mm), binarized and registered to FreeSurfer's average cortical surface (fsaverage) using surface-based registration (Fischl, 2012). The ventral endpoints were compared with a cytoarchitectonic atlas of the ventral occipital cortex (Rosenke et al., 2018). The dorsal endpoints were compared with a functional topographic atlas of the visual cortex (Wang et al., 2015). Following Takemura et al. (2016), we calculated for each cortical region the VOF coverage, defined as the proportion of voxels in close proximity to VOF endpoints. In short, we projected the streamlines' endpoints onto the cortex using a 3D Gaussian smoothing kernel (3 mm). We used FreeSurfer's surface-based registration to register the ROI masks of each atlas to the subjects' T1 space, and then warped them to diffusion space using the calculated warp for the T1 map. We then calculated the proportion of ROI voxels that intersected with the smoothed VOF endpoints.

We repeated the cortical endpoints analysis spatially-based methods for VOF identification in the subset of young adults (n = 32).

2.13. Microstructural changes in the VOF across the lifespan

To study how the microstructural properties of VOF-T1 and pAF change across the lifespan, we modeled the change in R1 (1/T1), MD and FA as a function of age (see Appendix D).

2.14. VOF identification using other quantitative MRI parameters

We tested whether the VOF can be identified using other quantitative MRI parameters (MD, FA or quantitative T2). To account for the different spatial resolutions, we additionally used a downsampled version of the T1 map to match the resolution of the other parameter maps (2 mm isotropic). To minimize the difference between the T1 and the non-T1 pipelines, we excluded any voxel that was excluded when using T1.

For the diffusion-based parameters, we used the cohort of 32 young adults from the main dataset. Eight hemispheres with very sparse candidate streamlines (<300) were excluded, resulting in 56 hemispheres. For the use of T2, we used the HUJI dataset.

To assess the robustness of the separation based on each quantitative MR parameter, we defined the separation effect size for each parameter (T1/MD/FA) as follows:

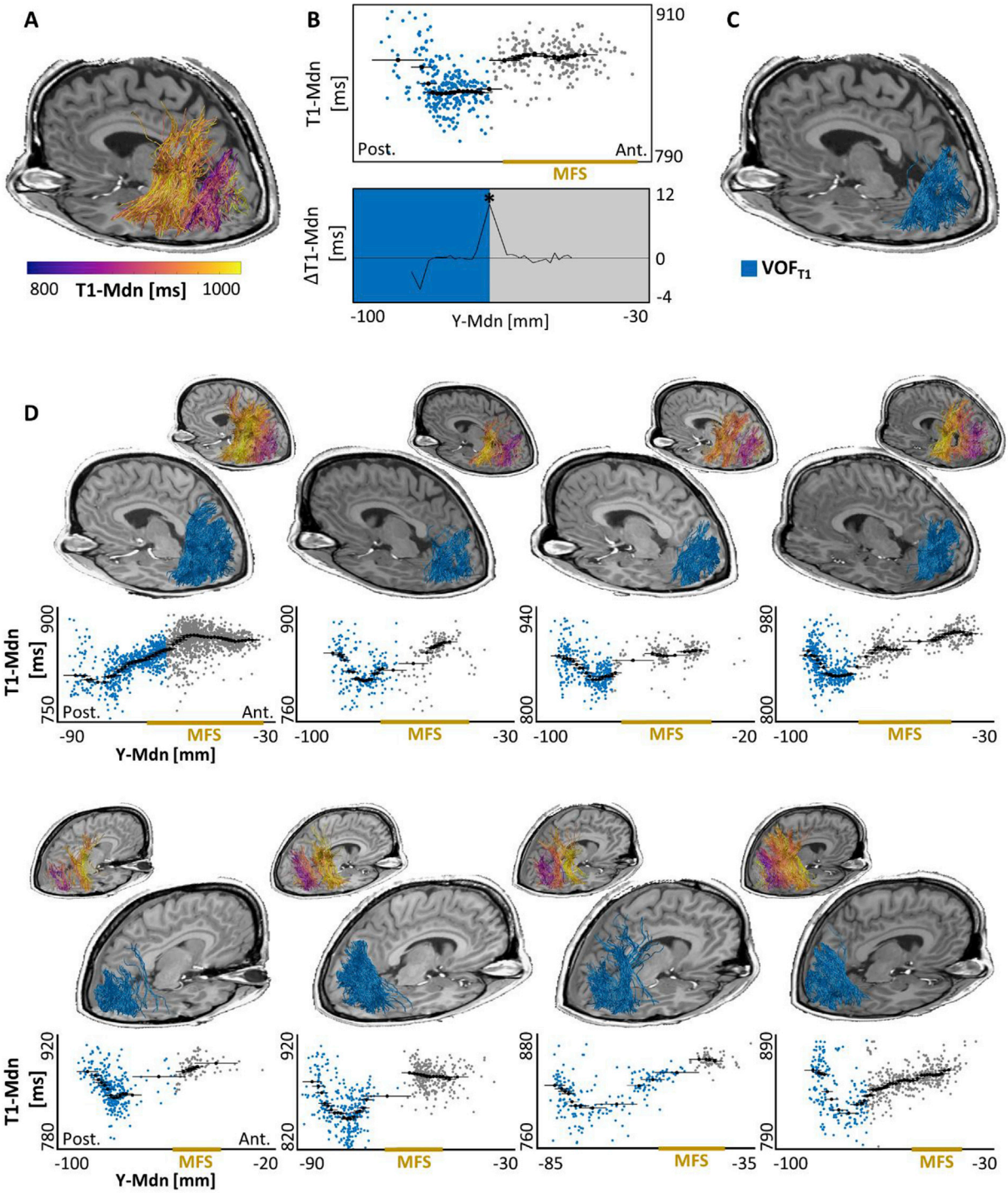

Fig. 4. T1-based identification of the VOF. (A) The candidate vertical streamlines in an example subject, colored by their T1-Mdn value. The posterior portion of these streamlines typically have lower T1-Mdn values. Streamlines excluded from the T1 analysis due to B1+ extrapolation are not shown. **(B)** The T1-based identification procedure. Top: The border between the VOF (blue) and the more anterior candidate streamlines was chosen as the point of sharpest increase in T1 values along the posterior-anterior axis (x-axis), close to the posterior end of the mid-fusiform sulcus (MFS, ochre line). Bottom: The T1-difference was calculated between the median values (black circle) in consecutive overlapping windows (black horizontal lines). Individual streamlines are represented by filled circles. **(C)** The resulting bundle, VOF-T1. **(D)** Example of the T1-based identification procedure in eight subjects for left (top) and right (bottom) hemispheres. Ant. anterior. Post. posterior.

$$separation\ effect\ size = \frac{Mdn(\mathrm{T1/MD/FA})_{ant.3} - Mdn(\mathrm{T1/MD/FA})_{post.3}}{Mdn(\mathrm{T1/MD/FA})_{ant.3}}$$

where $Mdn(\mathrm{T1/MD/FA})_{ant.3}$ is the median parameter value of the streamlines in the three bins anterior to the border and $Mdn(\mathrm{T1/MD/FA})_{post.3}$ is the median parameter value of the streamlines in the three bins posterior to the border. We compared the separation effect size for all cases in which the diffusion-based border was found in proximity to the T1-based border (within 5 mm).

2.15. Code availability

All code for T1-based VOF identification, with example data, is publicly available as open source MATLAB code (https://github.

com/MezerLab/VOF-T1).

3. Results

3.1. Microstructural and macroanatomical observations in VOF and pAF

The VOF and the pAF are vertical white-matter pathways originating from the vOTC, just lateral to the sagittal stratum. We observed that in multiple cases, the white-matter voxels that correspond to the VOF and pAF show distinct T1 values, with the more posterior cluster of voxels showing lower T1 values (Fig. 3B; Sup. Fig. 1). To further investigate these signatures, we used diffusion MRI tractography to reconstruct the VOF and pAF using published methods. The reconstructed VOF and pAF show distinct T1 values. The median T1 across each tract was lower in the VOF compared with the pAF (Fig. 3C; mean ± STD VOF-waypoint: 845 ± 33 ms; VOF-anatomy: 844 ± 32 ms; pAF: 866 ± 26 ms). Furthermore, within hemisphere, the difference between the median T1 in the pAF and in the VOF was significantly greater than zero (Fig. 3D), both for VOF-anatomy (median ± MAD (median-absolute-deviation) Left: 26 ± 17 ms; Right: 30 ± 11 ms; $p < 10^{-6}$ for both hemispheres in a one-tailed paired samples Wilcoxon test) and VOF-waypoint (Left: 29 ± 16 ms; Right: 43 ± 13 ms; $p < 10^{-9}$). The mean T1 profiles along each tract are presented in Fig. 3E and F. These results allow us to hypothesize that the VOF and pAF present distinct microstructural signatures, with a similar trend as that found in the vOTC (Lerma-Usabiaga et al., 2018).

3.2. T1-based identification of the VOF

To test if we can delineate the VOF using T1 mapping, we first used diffusion MRI tractography to identify a candidate set of vertical streamlines originating in the vOTC (Fig. 4A,D). In the cases of spatially separated bundles, we noticed that the anterior end of the VOF (the more posterior bundle) lies in close proximity to the posterior end of the mid-fusiform sulcus (MFS; Fig. 1C, Sup Fig. 2). Visual inspection revealed that the posterior and anterior portions of the candidate streamlines differ in their T1 signature. Fig. 4A shows the candidate streamlines in one subject, colored by the median T1 value along their length (T1-Mdn). More posterior candidates are characterized by lower T1-Mdn values, suggesting greater myelin content. This result agrees with previous histological studies that showed that greater myelin content in early sensory regions compared with cross-modal regions (e.g., the parietal lobe; Nieuwenhuys and Broere, 2017). The same pattern is evident in all subjects (see additional examples in Fig. 4D). We therefore used the streamlines' T1-Mdn value to determine the border separating the posterior streamlines from the anterior ones. We term the resulting posterior bundle VOF-T1.

When plotting the T1-Mdn values of the candidate streamlines against their median position along the posterior-anterior axis (Y-Mdn), a sharp increase in T1 values from posterior to anterior can be seen in the majority of the subjects (Fig. 4B,D). The anterior border of the VOF was determined as a point of sharp increase in T1-Mdn. Since the use of a single extremum is prone to be noise-sensitive, we identified the two sharpest increases in T1-Mdn, and chose the one closer to the posterior end of the MFS. As no ground truth exists for *in vivo* tractography, we assessed the quality of the resulting tract in comparison to previous descriptions of the VOF, based on subjective visual inspection. In particular, cases in which the VOF included multiple anterior streamlines projecting to the temporo-parietal junction or the superior parietal lobe were deemed unsuccessful. Using the T1-based algorithm, we successfully identified the VOF in 88/89 left hemispheres and 83/89 right hemispheres (for more quantitative analysis, see below). We found a tendency for greater volume in the right VOF-T1 (7.84 ± 3.09 ml) compared with the left VOF-T1 (6.64 ± 3.39 ml; $p = 0.014$, paired-sample *t*-test). For an additional, quantitative analysis, see below (*Comparison with anatomically defined VOF*).

We verified that the proposed algorithm is robust with respect to changes in the underlying parameters (see Appendix C). In addition, we tested whether other quantitative MRI parameters (T2, FA or MD) also can be used for VOF delineation. We found that while they can be used as informative input, the best results are obtained using T1 (Sup. Figs. 14 and 15).

3.3. Controlling for instrumental biases

Next, we wanted to rule out an alternative source that could potentially explain the VOF separation by T1-Mdn values, i.e., a gradient of B1+ excite field inhomogeneity along the posterior-anterior axis. First, we observed that in multiple subjects, plotting the candidate streamlines T1-Mdn against their posterior-anterior position resulted in two distinct and stable clusters, and not in a gradually increasing continuum of T1-Mdn values, as would be expected with a slowly varying bias field (Fig. 4). Second, we repeated the VOF separation in a single subject scanned three times for T1 mapping, each time with the head tilted at a different angle. Tilting the head leads to a different spatial distribution of B1+ inhomogeneity. While the three scans demonstrated different B1+ inhomogeneity fields (Sup. Fig. 3B), the resulting separations of the VOF were almost identical (Sup. Fig. 3C). These results provide evidence that the distinct T1 signatures of the VOF and the more anterior vertical candidates reflect true microstructural variation, and are not a result of instrumental biases.

3.4. Scan-rescan reliability

To assess the scan-rescan reliability, we repeated the T1-based VOF delineation process in four subjects, scanned twice for the full protocol. Supplementary Figures 4–7 show the scan-rescan results for these subjects. The anterior-posterior T1 profiles are very similar across scans, suggesting good scan-rescan reliability of the resulting VOF-T1. In one left hemisphere (subject 2; Sup. Fig. 5A) and two right hemispheres (subjects 1 and 3; Sup. Figs. 4E and 6E) we noticed a sub-bundle of streamlines that were excluded from VOF-T1 in the first scan and included for the second scan. This indicates that while the T1 map holds valuable information for VOF identification, the proposed algorithm may be sensitive to small changes in the input, especially in cases where two sharp increases in T1 appear close to the posterior end of the MFS. In such cases, the anterior-posterior T1 profile can aid in a manual segmentation of the VOF (as was done in Sup. Fig. 4E' and 6E').

3.5. The T1 signature of VOF-T1

The proposed procedure for identifying VOF-T1 is based on a local change in T1 values, and does not guarantee that VOF-T1 will show a signature of low T1 throughout its extent. We therefore quantitatively compared the T1 signatures of VOF-T1 and pAF. As in the case of the two spatially-based identification methods of the VOF (Fig. 3), VOF-T1 shows a signature of low T1 compared with the pAF throughout its extent (Fig. 3E and F; Sup. Fig. 8). The median T1 of VOF-T1 (mean ± STD 845 ± 33 ms) was lower compared to the pAF (866 ± 26 ms; Fig. 3C). Furthermore, the difference between the median T1 of the pAF and that of VOF-T1 was significantly greater that zero across hemispheres (median ± MAD Left: 26 ± 18 ms; Right: 30 ± 12 ms; $p < 10^{-6}$ for both hemispheres in a one-tailed paired samples Wilcoxon test; Fig. 3D).

3.6. Comparison with spatially-defined VOF

As in any *in vivo* tractography study, the lack of ground truth limits the possibility to fully validate the results. Therefore, to estimate the validity of our T1-based VOF delineation, we used the cohort of young adult subjects and compared our results with two published methods for VOF delineation, based on spatial criteria: VOF-anatomy and VOF-waypoint. We quantified the voxel-wise agreement between the methods by

calculating the Dice coefficient between the resulting tracts (Fig. 5A). VOF-T1 showed high agreement with VOF-anatomy (mean ± STD Dice coefficient across subjects: 0.88 ± 0.1), and low agreement with VOF-waypoint (0.4 ± 0.2). The volume of the resulting tracts was also comparable across methods, with the greatest volumes found for VOF-waypoint (Fig. 5B; Table 1).

We used LiFE to evaluate the strength of evidence (S; Caiafa and Pestilli, 2017; Pestilli et al., 2014) for the VOF, as identified by each method. Here too, we found comparable values across methods, with greater values found for VOF-waypoint. As described before, the difference in S values can be attributed in part to the volume differences, as larger tracts tend to result in greater S values (Pestilli et al., 2014).

Finally, we quantified the fraction of pAF voxels traversed by VOF streamlines, which should be minimal. The percent of pAF voxels traversed by VOF-T1 (of the total pAF voxels traversed by the candidate streamlines) was very small, and was lower for the left hemisphere (mean ± STD 0.6% ± 2%) compared with the right (2.5% ± 4.3%; Fig. 5C). This difference was statistically significant ($p < 0.01$; paired-sample *t*-test, $n = 32$). We found that this difference could not be explained by a volume laterality in the pAF. The volume of the pAF tended to be greater in the left hemisphere (mean ± STD 18.0 ± 5.8 ml) than in the right hemisphere (17.4 ± 6.0 ml), but this difference was not statistically significant ($p = 0.2$, paired samples *t*-test).

3.7. Cortical endpoints of the VOF

Fig. 6A shows the cortical endpoints of the VOF-T1 (heatmap) compared with those of the entire candidate set of vertical streamlines (dark blue) across the entire population ($n = 89$). Candidate streamlines projecting to the temporo-parietal region were consistently eliminated by the proposed T1-based procedure. The eliminated streamlines share much of their course with the anatomically defined pAF, but they differ from the pAF in two ways: their trajectory is less curved, and some of them reach the superior parietal lobule (Sup. Fig. 9).

To study the cortical endpoints of VOF-T1, we compared them with published atlases (Fig. 6B): a cytoarchitectonic atlas of the ventral occipital cortex (Rosenke et al., 2018) and a functional topographic atlas of the visual cortex (Wang et al., 2015). Interestingly, while VOF-T1 is defined based on T1 values within the white matter, the resulting projection sites respect the cortical parcellations of cytoarchitectonic and functional atlases (Fig. 6B). Dorsally, VOF-T1 projects most consistently to the functionally-defined areas V3A and V3d, as well as to IPS0 and IPS1. Ventrally, it terminates most consistently in the cytoarchitectonic areas hOc3v and hOc4v, and to a lesser degree in the posterior parts of FG1 and FG2.

Fig. 6C–E shows for each cortical region the proportion of voxels within 3 mm from VOF-T1 streamline endpoints. Dorsally, the most covered region is V3A, followed by V3d. Ventrally, we found greater coverage by the cytoarchitectonic atlas, with the greatest proportion of voxels found for FG2 and hOcv4.

The implications for the function of the VOF are discussed below (see Discussion).

Using the subset of young adults, we found that while VOF-T1 and VOF-anatomy present similar cortical projections, they differ from the results obtained for VOF-waypoint (Fig. 7). Notably, streamlines of VOF-anatomy tend to terminate in more lateral cortical regions, such as V3B, LO1 and LO2, and to have fewer terminations in IPS1 anteriorly, and V2d posteriorly.

3.8. Microstructural changes in the VOF across the lifespan

We wanted to study how microstructural signatures of VOF-T1 and pAF change throughout the lifespan (see Appendix D). In short, we calculated the median R1 (1/T1), MD or FA for each tract. Following previous literature (Yeatman et al., 2014a), we fit a quadratic model of R1 as a function of age and a Poisson model of the diffusion-based parameters as a function of age (Sup. Fig. 13). We found that VOF-T1 and pAF indeed show inverted U-shaped trajectories of R1 throughout the lifespan, whereas MD follows a Poisson curve, as reported for other white-matter tracts (Yeatman et al., 2014a). We note that compared with VOF-T1, pAF shows consistently lower R1 throughout the lifespan. This agrees with our observation of higher T1 (i.e., lower R1) in anterior streamlines (like pAF; Figs. 3 and 4), and further confirms the applicability of the proposed method across the lifespan.

3.9. The distinct T1 signatures of the VOF and pAF

Our proposed method relies on identifying a local difference in the T1 between the VOF and more anterior streamlines. We tested if the VOF-T1 and pAF present distinct T1 signatures throughout their extent, and found that 80% of the analyzed hemispheres (129/163) showed the expected effect (lower T1 in the VOF). A one-tailed *t*-test on the mean T1 of those hemispheres revealed that this difference was statistically significant in 95% of the hemispheres (122/129; alpha = 0.05, adjusted for Bonferroni correction).

3.10. VOF identification using other quantitative MRI parameters

We tested whether the VOF can be identified using other quantitative MRI parameters. Fig. 8A compares the Dice coefficient (quantifying the spatial overlap with VOF-anatomy) for different MR parameters. On average, the highest Dice coefficient values were found for T1 (mean ± STD 0.88 ± 0.11), followed by T1-downsampled (0.87 ± 0.09), FA (0.80 ± 0.18) and MD (0.80 ± 0.18). As evident by the standard deviation of the results, the diffusion-based parameters also showed greater variability in the Dice coefficient values across subjects. In a one-tailed paired-samples *t*-test between T1-downsampled and each of the other parameters (Bonferroni corrected for multiple comparisons), no significant difference was found between T1 and T1-downsampled ($p > 0.05$), while a significant difference was found in comparison of T1-downsampled with FA ($p < 0.05$) and MD ($p < 0.01$). These results suggest that the T1 sensitivity for VOF delineation remains also when using lower resolution (2 mm^3).

While the results are not as robust as in the case of T1, the resulting MD-border in 22/56 hemispheres (39%) was within 5 mm from the T1-based border (mean ± STD distance between borders 7 ± 6 mm). Similar results were found for the FA-based border (20/56 hemispheres (36%), mean ± STD distance between borders 10 ± 12 mm). For cases in which the T1-and MD-based borders were within 5 mm from each other, the separation effect size was greater for T1 (mean ± STD 0.022 ± 0.011) compared with MD (0.002 ± 0.013). For cases in which the T1-and FA-based borders were within 5 mm from each other, the average separation effect size was greater for FA, although this effect size was much more variable across hemispheres (T1 effect size: 0.027 ± 0.015; FA effect size: 0.040 ± 0.074).

Fig. 8B shows the distribution of Dice coefficient values for the use of T1, T1-downsampled and T2. Here, too, we found that the agreement with VOF-anatomy was greatest when using T1 (mean ± STD 0.77 ± 0.23), followed by T1-downsampled (0.74 ± 23) and finally T2 (0.63 ± 0.28). In a one-tailed paired-samples *t*-test between T1-downsampled and each of the other parameters (Bonferroni corrected for two comparisons), no significant difference was found between T1 and T1-downsampled ($p > 0.05$), while a significant difference was found in comparison of T1-downsampled with T2 ($p < 0.05$). For T2, the resulting border was within 5 mm from the T1-based border only in 7/28 hemispheres.

4. Discussion

In this study, we found strong evidence that white-matter tract delineation of the VOF *in vivo* can be facilitated by integrating diffusion MRI tractography with quantitative T1 mapping. We showed that the

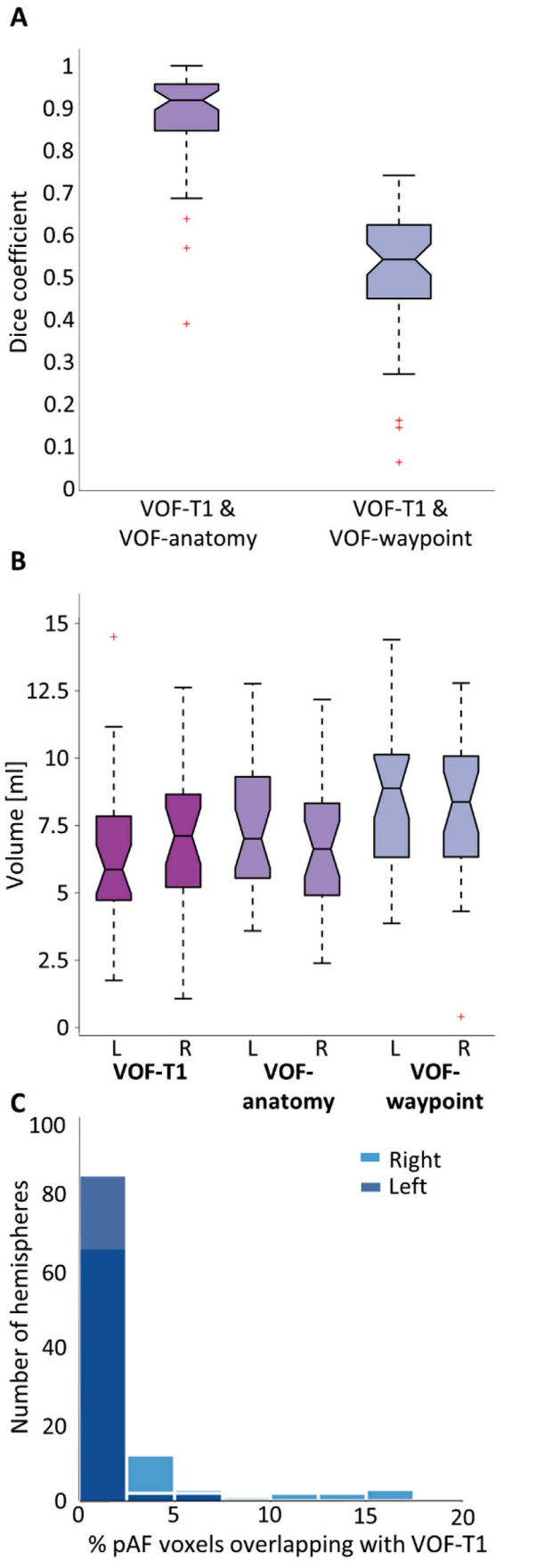

(caption on next column)

Fig. 5. Comparison with spatially-defined VOF. (A) Boxplots indicate the Dice coefficient of VOF-T1 calculated with each spatially-defined VOF, showing high agreement with VOF-anatomy (mean ± STD 0.88 ± 0.1). Center lines indicate median values; notch indicates 95% confidence interval for the median; box limits indicate the interquartile range (IQR; 25th-75th percentiles); whiskers extend to the most extreme data points within 1.5 x IQR outside the box. Cases outside this range are individually represented as red crosses. **(B)** Boxplots indicate the VOF volume per hemisphere, showing comparable results across methods. **(C)** The histogram shows the percentage of candidate voxels that overlap with the pAF, and were traversed by streamlines included in VOF-T1. As expected, this percentage was low both for the left (0.5% ± 1%) and right (3% ± 4%) hemispheres.

candidate set of vertical streamlines originating in the vOTC includes two clusters that can be separated based on a sharp increase in their T1 signatures. We implemented this observation as an observer-free procedure for determining a separating border on the posterior-anterior axis. This procedure results in a posterior group of streamlines, which we term VOF-T1. Previous studies have identified the VOF based on spatial criteria, using white-matter waypoint ROIs (Keser et al., 2016; Takemura et al., 2016), using cortical ROIs (Briggs et al., 2018) or requiring no intersection with an independently defined pAF (Weiner et al., 2016). To this family of methods we add an approach that is inspired by algorithms used in quantitative cytoarchitectonics, where a border between two cortical regions is based on a sharp change in the profile of cell packing density along the cortex (Schleicher et al., 1998). Here we build on the assumption that different tracts have distinct microstructural properties. We were able to reconstruct the VOF-T1 in 171/178 hemispheres (88/89 in the left hemispheres), in subjects 7–85 years old. While the proposed procedure is heuristic in nature, we have shown that it is reliable using scan-rescan data, and that it is robust to changes in various tuning parameters (see Appendix C). Nevertheless, it is possible that some parameters have to be tuned when applying the proposed method to another data set, or using other preprocessing steps in the analysis. The choice of registration method of the T1 map to the diffusion data could also affect the analysis results (see Appendix B). Future work could further characterize the effects of different registration methods.

The myelin-sensitive T1 is known to vary between white-matter tracts (De Santis et al., 2014; Schurr et al., 2018; Yeatman et al., 2014a). Previous works compared the VOF with other tracts within the occipital lobe, and found that it shows less myelin staining (Forkel et al., 2014) and higher T1 values (Yeatman et al., 2014b). Here we identified an additional T1 difference between VOF and the white matter outside the occipital lobe, in the temporo-parietal region. These findings agree with a posterior-anterior T1 pattern that was recently described in the ventral cortical projection sites of the VOF and pAF (Lerma-Usabiaga et al., 2018). These distinct T1 signatures could have several underlying biological sources. While T1 is sensitive to myelin, it is also affected by factors such as water content (Mezer et al., 2013), iron content (Gelman et al., 2001; Stüber et al., 2014), mean axonal diameter (Harkins et al., 2016), inflammation (Stanisz et al., 2004), edema (Bastin et al., 2002) and axonal loss (Brex et al., 2000). Therefore, care must be taken when applying the proposed method in pathological cases (e.g., in case of focal lesions; see Dayan et al., 2016; Schurr et al., 2018). In particular, the accuracy of VOF identification might be compromised in case the pathology differentially affects one of the white-matter tracts, thereby decreasing the T1 contrast between them.

The cortical endpoints of VOF-T1 may inform us about the tract's functional role in the communication between ventral and dorsal visual streams. The cortical endpoints of VOF-T1 agree with both functional and cytoarchitectonic parcellations of the ventral and dorsal cortices. The dorsal VOF-T1 endpoints are most consistent across subjects in the functional areas V3A and V3d. V3A is the first region in the visual cortex to include a full map of the entire hemifield, which makes the VOF a good candidate for communicating information between the ventral and dorsal visual streams (Takemura et al., 2016). Dorsally, the VOF also projects

Table 1
Quantitative comparison of tract volume and strength of evidence (S, as evaluated by LiFE) for the three VOF identification methods (mean ± STD; n = 32 subjects).

	VOF-T1		VOF-anatomy		VOF-waypoint	
	L	R	L	R	L	R
Strength of evidence]s.d.[	0.6 ± 0.4	0.9 ± 0.6	0.7 ± 0.4	1.0 ± 0.6	1.0 ± 0.4	2.0 ± 1.2
Volume]ml[	6.4 ± 2.8	6.9 ± 2.7	7.3 ± 2.3	7.0 ± 2.7	8.6 ± 2.4	8.0 ± 2.8

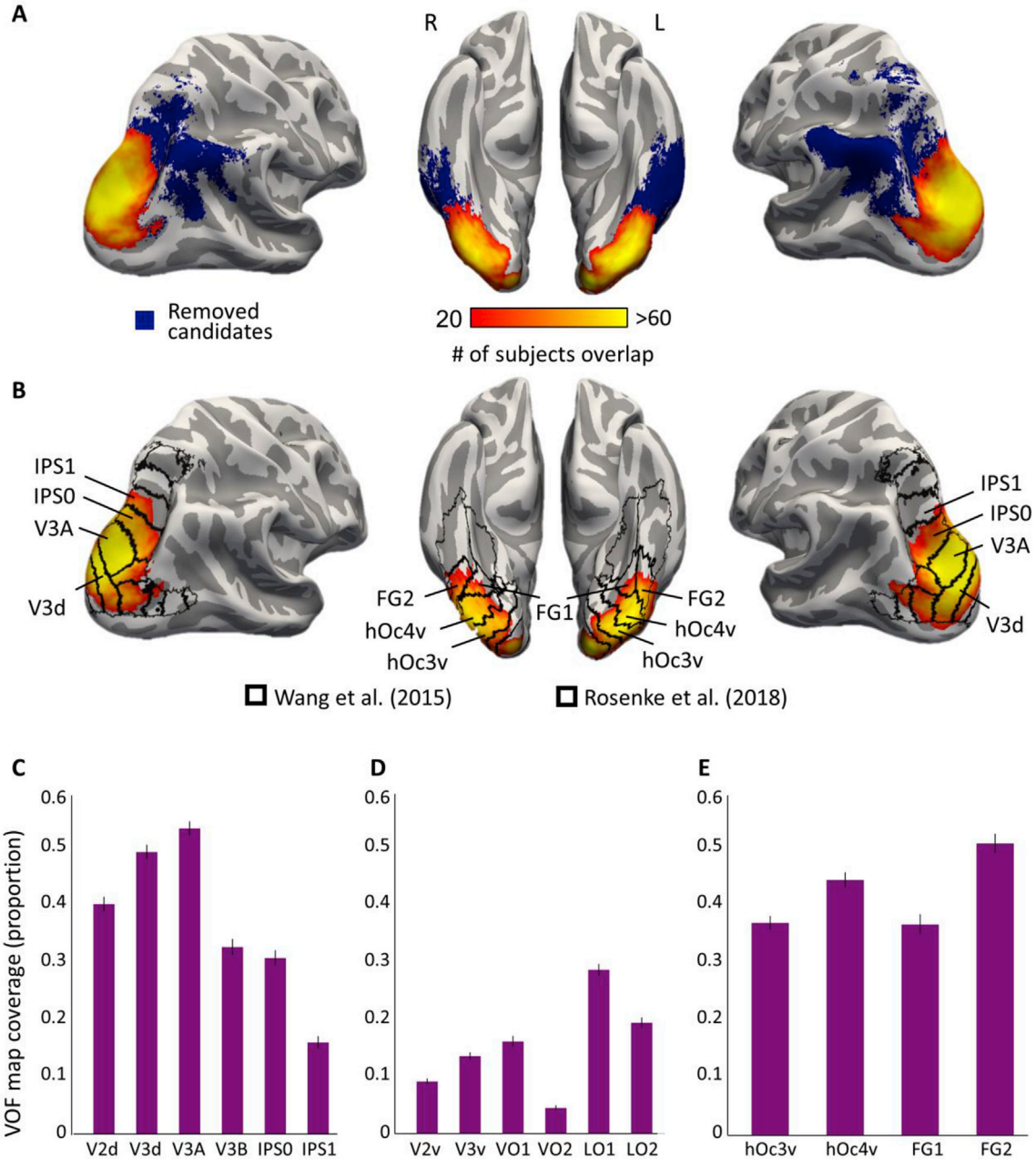

Fig. 6. Cortical endpoint of VOF-T1. (A) The cortical projections of VOF-T1 overlaid on the inflated average cortical surface in MNI space, shown from dorsal (left, right) and ventral (middle) points of view. The cortical projections are consistent across subjects (left: n = 88, right: n = 83). Blue regions mark cortical projections that were consistent across subjects (n>=20) but were removed in the process of T1-based VOF identification. **(B)** The same cortical projections shown with regions-of-interest borders for the Wang et al. (2015) functional atlas of visual topography (left, right) and for the Rosenke et al. (2018) cytoarchitectonic atlas (middle). Ventrally, VOF-T1 projects mainly to hOc3v-4v and the posterior parts of FG2. Dorsally, VOF-T1 projects mainly to V3a and V3d, as well as IPS0. **(C-E)** Bar plots indicating the proportion of voxels within 3 mm from VOF-T1 streamline endpoints for the atlases of Wang et al. (C-D) and Rosenke et al. (E). Error bars indicate ±SEM. hOc: Human occipital cytoarchitectonic area. hOcv: Ventral human occipital cytoarchitectonic area. IPS: *Intraparietal sulcus*.

to IPS0 and IPS1 regions, which have been shown to communicate information between the two visual streams (Kay and Yeatman, 2017). In the ventral visual cortex, we found that VOF-T1 terminates most consistently in the cytoarchitectonic areas hOc3v and hOc4v. VOF-T1 also terminated in the posterior parts of FG1 and FG2, which include face-selective and character-selective regions (Weiner et al., 2017). Our results corroborate a recent study that found different functional responses within the left vOTC to written words stimuli (Lerma-Usabiaga

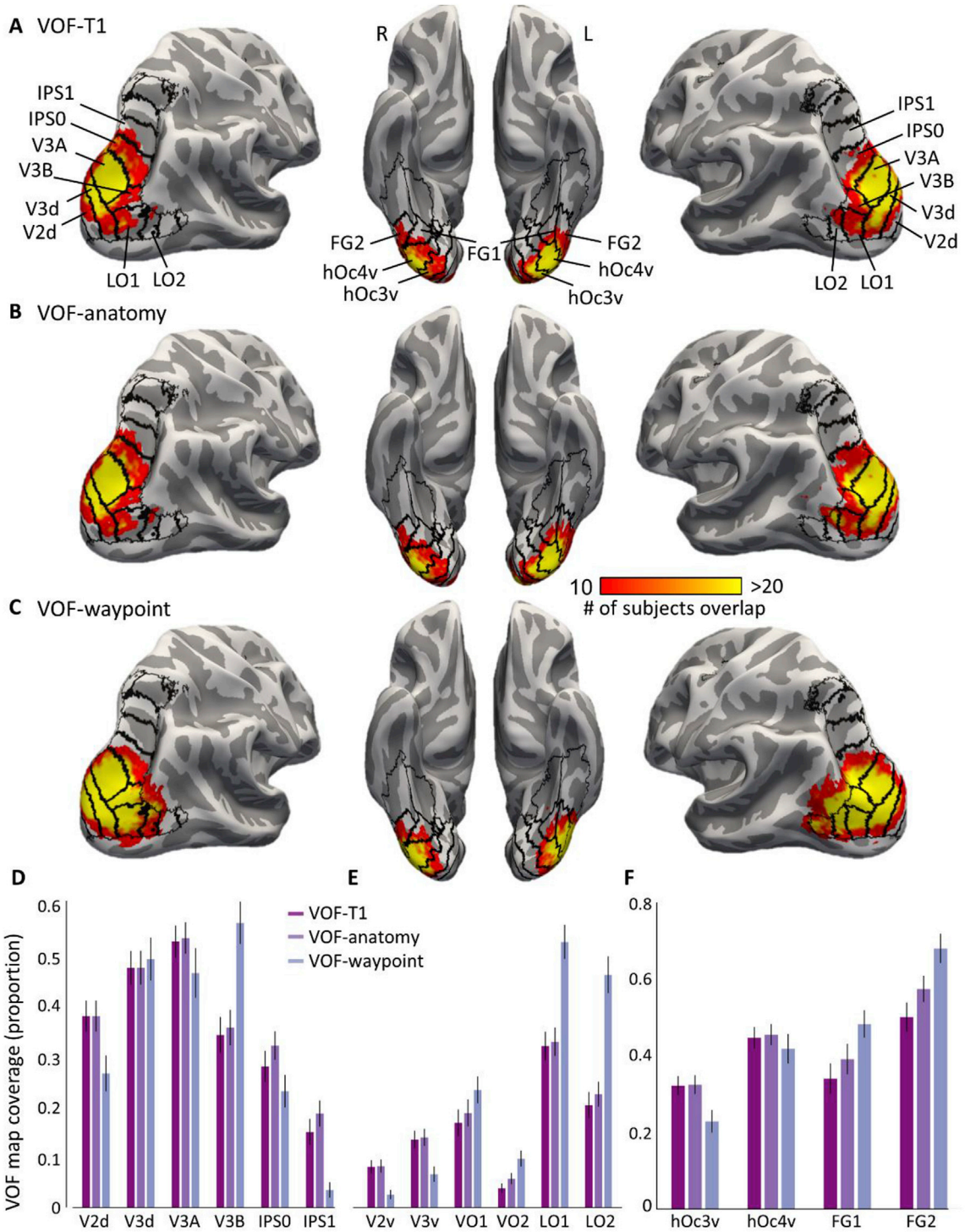

Fig. 7. Cortical endpoints of VOF across identification methods. The cortical projections of the VOF across the young adults (n = 32) overlaid on the inflated average cortical surface in MNI space, shown from dorsal (left, right) and ventral (middle) points of view. Results are shown for **(A)** VOF-T1, **(B)** VOF-anatomy and **(C)** VOF-waypoint, with regions-of-interest borders for the Wang et al. (2015) functional atlas of visual topography (left, right) and for the Rosenke et al. (2018) cytoarchitectonic atlas (middle). While VOF-T1 and VOF-anatomy result in a very similar pattern of cortical endpoints, streamlines of the VOF-waypoint method tend to terminate in more lateral regions such as V3B, LO1 and LO2. By construction, VOF-waypoint streamlines are more confined to the occipital lobe, with fewer projections reaching IPS1. **(D-F)** Quantitative analysis of the VOF cortical endpoints across identification methods. Bar plots indicating the proportion of voxels within 3 mm from VOF-T1 streamline endpoints for the Wang et al. functional atlas **(D-E)** and the Rosenke et al. cytoarchitectonic atlas **(F)**. Error bars indicate ±SEM.

et al., 2018). These results are also in line with our findings regarding the spatial relationship of VOF-T1 and the MFS. Others have shown that the MFS can be used as an anatomical landmark for identifying functional regions (Weiner et al., 2014). A previous study (Yeatman et al., 2014b) used a common reference space and reported that the anterior boundary of the anatomically-defined VOF usually occurs near the middle of the MFS. We identified the MFS in individual subjects and found that the sharp increase in T1 tends to occur in close proximity to the posterior end of the MFS. Therefore, when our algorithm has to choose between two possible T1-based borders, it prefers the one closer to the posterior end of

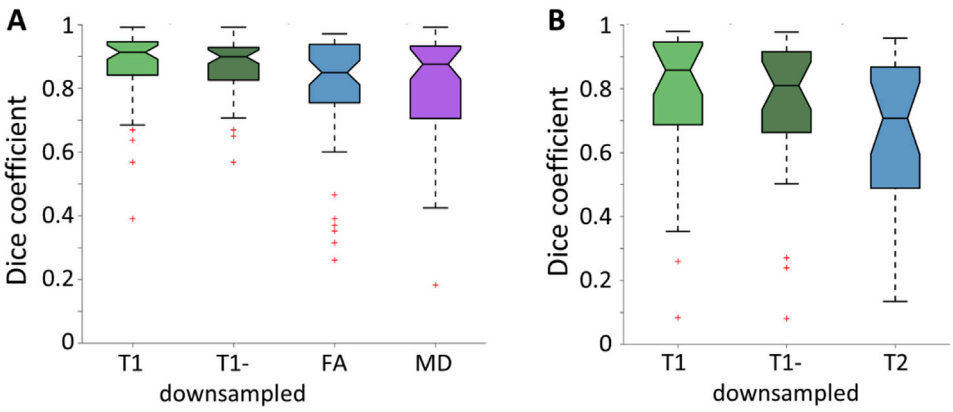

Fig. 8. Dice coefficient of VOF delineation using different MR parameters. (A) Boxplots indicate the distribution of Dice coefficient values (quantifying the agreement with VOF-anatomy) across analyzed hemispheres of young adults in the main dataset (n = 54 hemispheres). The T1-based delineation results in greater Dice coefficient values compared with diffusion-based parameters. This difference is significant in a one-tailed paired-samples *t*-test between T1-downsampled and each of the diffusion-based parameters ($p < 0.05$). **(B)** In the HUJI dataset (n = 26 hemispheres), T1 results in greater Dice coefficient values compared with T2 ($p < 0.05$). Center lines indicate median values; notch indicates 95% confidence interval for the median; box limits indicate the interquartile range; whiskers extend to the most extreme data points within 1.5 x IQR outside the box. Cases outside this range are individually represented as red crosses.

the MFS. This supports previous work that advocated the integration of microstructural and macrostructural priors for resolving cases of ambiguity in tractography (Daducci et al., 2016, 2015; Jbabdi et al., 2015; Schurr et al., 2018). Another source of information that could potentially be used for separating VOF and pAF is the distinct T1 signature of their cortical endpoints (Lerma-Usabiaga et al., 2018). Such additional information could be useful for mitigating the limitations of tractography algorithms near the cortex, where the diffusion signal is less coherent (Jbabdi and Johansen-Berg, 2011).

As in any *in vivo* tractography study, the lack of ground truth limits the ability to validate the results. Here we chose to compare our proposed procedure with two published methods for VOF identification, both based on spatial criteria: (1) VOF-anatomy, which builds on the identification of the well-defined pAF, and requires no intermingling between the two tracts (Weiner et al., 2016; Yeatman et al., 2014b), and (2) VOF-waypoint, which is based on defining two waypoint ROIs within the occipital white matter (Takemura et al., 2016). Our results suggest a high level of agreement between VOF-T1 and VOF-anatomy, in terms of their spatial overlap, T1 signatures, volume, strength of evidence (S) and pattern of cortical projections. In part, this agreement can be attributed to the fact that both tracts are subsets of the same candidate set of vertical streamlines. This is in contrast to VOF-waypoint, which showed less agreement with VOF-T1 in all these aspects. In particular, we found that the choice of tract identification method affects the resulting cortical endpoints (Bain et al., 2019), such that the cortical endpoints of VOF-waypoint tend to cover more lateral regions: V3B, LO1 and LO2. These discrepancies can be traced back to the underlying methodological choices of each method, e.g.: VOF-anatomy excludes streamlines shorter than 20 mm, as well as streamlines that do not travel vertically for most of their path; VOF-waypoint is restricted to the occipital white matter, while VOF-anatomy is not. We note that the proposed T1-based identification of the VOF is less conservative in terms of the anterior extent of the VOF, as it does not pose restrictions on VOF intermingling with pAF. Here we found that in some cases, the reconstructed VOF-T1 and pAF do intermingle, albeit to a small degree. This is plausible according to the description of post-mortem dissections by Curran (1909), who described the VOF as extending "from the pole of the occipital lobe to the arcuate fibers". The existence of VOF as single bundle or as a collection of several sub-bundles is still an open question (Briggs et al., 2018; Forkel et al., 2014). The proposed VOF-T1 may therefore include other nearby vertical pathways such as the stratum cunei transversum and adjacent U-fibers (Forkel et al., 2014) that we could not reliably identify. Future work using higher resolution and additional MRI contrasts (Deoni and Kolind, 2015; Henkelman et al., 1993; Lee et al., 2012) may be able to shed more light on this question.

As for the eliminated anterior streamlines, we emphasize that we do not consider them as pAF necessarily. Previous accounts of the pAF describe it as an arched pathway, connecting posterior temporal and inferior parietal regions (Catani et al., 2005; Sandip et al., 2018). Indeed, the anterior streamlines we eliminate overlap extensively with the anatomically-defined pAF, yet do not cover all of it (Sup. Fig. 8). Furthermore, some of these anterior streamlines project to more superior parietal regions, and may correspond with a separate recently proposed pathway (Kamali et al., 2014). Therefore, when comparing VOF and pAF properties, we used an anatomically-based protocol designed specifically for pAF identification (Weiner et al., 2016).

A recent work that identified the VOF using deterministic tractography and a set of inclusion and exclusion regions of interest found no laterality in VOF volume (Keser et al., 2016). Here we observed some differences between the left and right VOF-T1. Our subjective visual assessment revealed more cases of unsuccessful VOF identification in the right hemisphere. Furthermore, we found a tendency for greater volume in the right VOF-T1, with a greater percentage of pAF voxels traversed by VOF-T1. The greater overlap with pAF in the right hemisphere could not be explained by laterality in the volume of the pAF. This is in line with previous work that found rightward volume laterality of the pAF only for young subjects 9–11 years old (Budisavljevic et al., 2015), or no volume laterality at all (Thiebaut de Schotten et al., 2011; but see Wilkinson et al., 2017). It is possible that there is no laterality effect in the actual volume of the VOF, and these results reflect a laterality effect in our ability to identify a border using the streamlines T1 profile.

Quantitative MRI techniques aim to provide unbiased microstructural parameter maps. Nevertheless, imperfections in the fitting procedure may lead to residual instrumental bias in the final maps. Here we wanted to rule out an alternative explanation that could account for the distinct T1 signature we observed between the posterior and anterior vertical streamlines. Specifically, it was shown that the B1+ excite field is characterized by a smoothly varying intensity, which might manifest as a local bias along the posterior-anterior axis. We found converging evidence against this alternative explanation (Fig. 4B, Sup. Fig. 3). Nevertheless, it is impossible to rule out the contribution of the instrumental bias, and additional validation such as post mortem quantitative myelin staining could be beneficial.

Different quantitative MRI techniques are sensitive to complementary aspects of the underlying tissue (De Santis et al., 2014; Mezer et al., 2013; Stikov et al., 2011; Yeatman et al., 2014a). In this work, we focused on quantitative T1 mapping and showed that it reveals a robust and reliable contrast between VOF and pAF. We further found that T1 gives better results compared with three other quantitative MRI parameters – MD, FA and T2. However, MD, FA and T2 do allow for some separation between

VOF and pAF. One explanation for this finding is that all these qMRI parameters are sensitive to similar or covarying microstructural properties of the VOF and pAF. A second explanation is the contribution of the macrostructural information (location of the MFS) to the proposed procedure. Third, partial volume effects may affect all the measured parameters near the VOF-pAF border, which tends to occur close to an intrusion of the superior temporal sulcus (STS; Fig. 3). In this region, the bundle of vertical fascicles is thinner compared with neighboring regions (Forkel et al., 2014). Other quantitative MRI parameters, such as T2*, myelin water fraction or quantitative magnetization transfer (Deoni and Kolind, 2015; Henkelman et al., 1993; Mackay et al., 1994), may provide additional sufficient contrast for separating the VOF. Further study of various quantitative MRI signatures of VOF and pAF could shed light on the biological sources of the observed contrast identified here. We hope that future studies will extend the approach presented here to other white-matter pathways, ultimately creating a multi-modal tractogram of the human white matter.

Acknowledgements

This work was supported by the ISF Grant (no. 0399306) and the NSF/SBE-BSF Grants (NSF no. 1551330 and BSF no. 2015608) awarded to A.A.M., and a seed grant from the Eric Roland Fund for Interdisciplinary Research administered by ELSC, awarded to A.A.M. and R.S. We thank Jesse Gomez and Kalanit Grill-Spector for providing data for testing reproducibility, their work was supported by NIH RO1EY02988-A1. We thank Brian Wandell for data collection, which was supported by the Weston Havens Foundation, NSF/BCS-1228397 and NIH EY015000. We thank Jason D. Yeatman, Hiromasa Takemura, Elizabeth Huber, Jonathan S. Bain and Franco Pestilli for helpful comments on this manuscript.

Appendix A. Supplementary data

Supplementary data to this article can be found online at https://doi.org/10.1016/j.neuroimage.2019.116121.

References

Andersson, J.L.R., Sotiropoulos, S.N., 2016. An integrated approach to correction for off-resonance effects and subject movement in diffusion MR imaging. Neuroimage 125, 1063–1078. https://doi.org/10.1016/J.NEUROIMAGE.2015.10.019.

Avants, B., Tustison, N., Song, G., 2009. Advanced normalization tools (ANTs). Insight J 2, 1–35.

Bain, J.S., Yeatman, J.D., Schurr, R., Rokem, A., Mezer, A.A., 2019. Evaluating arcuate fasciculus laterality measurements across dataset and tractography pipelines. Hum. Brain Mapp. hbm. 24626. https://doi.org/10.1002/hbm.24626.

Bammer, R., Zhang, B., Deng, W., Wiggins, G.C., Stenger, A.V., Sodickson, D.K., 2011. Impact of motion on parallel transmission. In: Proc 19th Scientific Meeting ISMRM, p. 4590.

Barral, J.K., Gudmundson, E., Stikov, N., Etezadi-amoli, M., Stoica, P., Nishimura, D.G., 2010. A robust methodology for in vivo T1 mapping. Magn. Reson. Med. 64, 1057–1067. https://doi.org/10.1002/mrm.22497.

Bastin, M.E., Sinha, S., Whittle, I.R., Wardlaw, J.M., 2002. Measurements of water diffusion and T1 values in peritumoural oedematous brain. Neuroreport 13, 1335–1340. https://doi.org/10.1097/00001756-200207190-00024.

Ben-Eliezer, N., Sodickson, D.K., Block, K.T., 2015. Rapid and accurate T2 mapping from multi-spin-echo data using Bloch-simulation-based reconstruction. Magn. Reson. Med. 73, 809–817. https://doi.org/10.1002/mrm.25156.

Berman, S., West, K.L., Does, M.D., Yeatman, J.D., Mezer, A.A., 2018. Evaluating g-ratio weighted changes in the corpus callosum as a function of age and sex. Neuroimage 182, 304–313. https://doi.org/10.1016/j.neuroimage.2017.06.076.

Brex, P.A., Parker, G.J., Leary, S.M., Molyneux, P.D., Barker, G.J., Davie, C.A., Thompson, A.J., Miller, D.H., 2000. Lesion heterogeneity in multiple sclerosis: a study of the relations between appearances on T1 weighted images, T1 relaxation times, and metabolite concentrations. J. Neurol. Neurosurg. Psychiatry 68, 627–632. https://doi.org/10.1136/JNNP.68.5.627.

Briggs, R.G., Conner, A.K., Sali, G., Baker, C.M., Burks, J.D., Glenn, C.A., Battiste, J.D., 2018. A Connectomic Atlas of the Human Cerebrum — Chapter 16: Tractographic Description of the Vertical Occipital Fasciculus, pp. 456–461. https://doi.org/10.1093/ons/opy270.

Budisavljevic, S., Dell'Acqua, F., Castiello, U., 2018. Cross-talk connections underlying dorsal and ventral stream integration during hand actions. Cortex 103, 224–239. https://doi.org/10.1016/j.cortex.2018.02.016.

Budisavljevic, S., Dell'acqua, F., Rijsdijk, F.V., Kane, F., Picchioni, X., Mcguire, P., Toulopoulou, T., Georgiades, A., Kalidindi, S., Kravariti, E., Murray, R.M., Murphy, D.G., Craig, M.C., Catani, M., 2015. Age-Related Differences and Heritability of the Perisylvian Language Networks. https://doi.org/10.1523/JNEUROSCI.1255-14.2015.

Bürgel, U., Amunts, K., Hoemke, L., Mohlberg, H., Gilsbach, J.M., Zilles, K., 2006. White matter fiber tracts of the human brain: three-dimensional mapping at microscopic resolution, topography and intersubject variability. Neuroimage 29, 1092–1105. https://doi.org/10.1016/j.neuroimage.2005.08.040.

Caiafa, C.F., Pestilli, F., 2017. Multidimensional encoding of brain connectomes. Sci. Rep. 7, 11491. https://doi.org/10.1038/s41598-017-09250-w.

Catani, M., Jones, D.K., Ffytche, D.H., 2005. Perisylvian language networks of the human brain. Ann. Neurol. 8–16. https://doi.org/10.1002/ana.20319.

Curran, E.J., 1909. A new association fiber tract in the cerebrum with remarks on the fiber tract dissection method of studying the brain. J. Comp. Neurol. Psychol. https://doi.org/10.1002/cne.920190603.

Daducci, A., Dal Palú, A., Descoteaux, M., Thiran, J.-P., 2016. Microstructure informed tractography: pitfalls and open challenges. Front. Neurosci. 10, 1–13. https://doi.org/10.3389/fnins.2016.00247.

Daducci, A., Dal Palu, A., Lemkaddem, A., Thiran, J.-P., 2015. COMMIT: convex optimization modeling for microstructure informed tractography. IEEE Trans. Med. Imaging 34, 246–257. https://doi.org/10.1109/TMI.2014.2352414.

Dayan, M., Monohan, E., Pandya, S., Kuceyeski, A., Nguyen, T., Raj, A., Gauthier, S., 2016. Profilometry: a new statistical framework for the characterization of white matter pathways, with application to multiple sclerosis. Hum. Brain Mapp. 37, 989–1004. https://doi.org/10.1002/hbm.23082.

De Santis, S., Drakesmith, M., Bells, S., Assaf, Y., Jones, D.K., 2014. Why diffusion tensor MRI does well only some of the time: variance and covariance of white matter tissue microstructure attributes in the living human brain. Neuroimage 89, 35–44. https://doi.org/10.1016/j.neuroimage.2013.12.003.

Deoni, S.C.L., Kolind, S.H., 2015. Investigating the stability of mcDESPOT myelin water fraction values derived using a stochastic region contraction approach. Magn. Reson. Med. 73, 161–169. https://doi.org/10.1002/mrm.25108.

Dice, L.R., 1945. Measures of the amount of ecologic association between species. Ecology 26, 297–302. https://doi.org/10.2307/1932409.

Duan, Y., Norcia, A.M., Yeatman, J.D., Mezer, A., 2015. The structural properties of major white matter tracts in strabismic amblyopia. Investig. Ophthalmol. Vis. Sci. 56, 5152–5160. https://doi.org/10.1167/iovs.15-17097.

Filo, S., Shtangel, O., Salamon, N., Kol, A., Weisinger, B., Shifman, S., Mezer, A.A., 2019. Disentangling molecular alterations from water-content changes in the aging human brain using quantitative MRI. Nat. Commun. 10, 3403. https://doi.org/10.1038/s41467-019-11319-1.

Fischl, B., 2012. FreeSurfer. Neuroimage 62, 774–781. https://doi.org/10.1016/j.neuroimage.2012.01.021.

Forkel, S.J., Mahmood, S., Vergani, F., Catani, M., 2014. The white matter of the human cerebrum: Part I the occipital lobe by Heinrich Sachs. Cortex 62, 182–202. https://doi.org/10.1016/j.cortex.2014.10.023.

Gelman, N., Ewing, J.R., Gorell, J.M., Spickler, E.M., Solomon, E.G., 2001. Interregional variation of longitudinal relaxation rates in human brain at 3.0 T: Relation to estimated iron and water contents. Magn. Reson. Med. 45, 71–79. https://doi.org/10.1002/1522-2594(200101)45:1<71::AID-MRM1011>3.0.CO;2-2.

Gomez, J., Barnett, M.A., Natu, V., Mezer, A., Palomero-gallagher, N., Weiner, K.S., Amunts, K., 2017. Microstructural proliferation in human cortex is coupled with the development of face processing. Science 355, 68–71.

Harkins, K.D., Xu, J., Dula, A.N., Li, K., Valentine, W.M., Gochberg, D.F., Gore, J.C., Does, M.D., 2016. The microstructural correlates of T 1 in white matter. Magn. Reson. Med. 75, 1341–1345. https://doi.org/10.1002/mrm.25709.

Henkelman, R.M., Huang, X., Xiang, Q.-S., Stanisz, G.J., Swanson, S.D., Bronskill, M.J., 1993. Quantitative interpretation of magnetization transfer. Magn. Reson. Med. 29, 759–766. https://doi.org/10.1002/mrm.1910290607.

Jbabdi, S., Johansen-Berg, H., 2011. Tractography: where do we go from here? Brain Connect. 1, 169–183. https://doi.org/10.1089/brain.2011.0033.

Jbabdi, S., Sotiropoulos, S.N., Haber, S.N., Essen, D.C., Behrens, T.E., 2015. Measuring macroscopic brain connections in vivo. Nat. Neurosci. 18, 1546–1555. https://doi.org/10.1038/nn.4134.

Jenkinson, M., Bannister, P., Brady, M., Smith, S., 2002. Improved optimization for the robust and accurate linear registration and motion correction of brain images. Neuroimage 17, 825–841. https://doi.org/10.1006/nimg.2002.1132.

Jenkinson, M., Smith, S., 2001. A global optimisation method for robust affine registration of brain images. Med. Image Anal. 5, 143–156.

Jones K., D., Horsfield A., M., Simmons, A., 1999. Optimal strategies for measuring diffusion in anisotropic systems by magnetic resonance imaging. Magnetic resonance in medicine 42 (3), 515–525.

Kamali, A., Sair, H.I., Radmanesh, A., Hasan, K.M., 2014. Decoding the superior parietal lobule connections of the superior longitudinal fasciculus/arcuate fasciculus in the human brain. Neuroscience 277, 577–583. https://doi.org/10.1016/j.neuroscience.2014.07.035.

Kay, K.N., Yeatman, J.D., 2017. Bottom-up and Top-Down Computations in Word- and Face-Selective Cortex 1–29. https://doi.org/10.7554/eLife.22341.

Keser, Z., Ucisik-Keser, F.E., Hasan, K.M., 2016. Quantitative mapping of human brain vertical-occipital fasciculus. J. Neuroimaging 26, 188–193. https://doi.org/10.1111/jon.12268.

Lee, J., Shmueli, K., Kang, B.-T., Yao, B., Fukunaga, M., van Gelderen, P., Palumbo, S., Bosetti, F., Silva, A.C., Duyn, J.H., 2012. The contribution of myelin to magnetic susceptibility-weighted contrasts in high-field MRI of the brain. Neuroimage 59, 3967–3975. https://doi.org/10.1016/j.neuroimage.2011.10.076.

Lee Masson, H., Wallraven, C., Petit, L., 2017. "Can touch this": cross-modal shape categorization performance is associated with microstructural characteristics of white matter association pathways. Hum. Brain Mapp. 38, 842–854. https://doi.org/10.1002/hbm.23422.

Lerma-Usabiaga, G., Carreiras, M., Paz-Alonso, P.M., 2018. Converging evidence for functional and structural segregation within the left ventral occipitotemporal cortex in reading. Proc. Natl. Acad. Sci. U.S.A. 201803003. https://doi.org/10.1073/pnas.1803003115.

Lutti, A., Dick, F., Sereno, M.I., Weiskopf, N., 2014. Using high-resolution quantitative mapping of R1 as an index of cortical myelination. Neuroimage 93, 176–188. https://doi.org/10.1016/j.neuroimage.2013.06.005.

Mackay, A., Whittall, K., Adler, J., Li, D., Paty, D., Graeb, D., 1994. In vivo visualization of myelin water in brain by magnetic resonance. Magn. Reson. Med. 31, 673–677. https://doi.org/10.1002/mrm.1910310614.

Mezer, A., Rokem, A., Berman, S., Hastie, T., Wandell, B.A., 2016. Evaluating quantitative proton-density-mapping. Methods 3635, 3623–3635. https://doi.org/10.1002/hbm.23264.

Mezer, A., Yeatman, J.D., Stikov, N., Kay, K.N., Cho, N.-J., Dougherty, R.F., Perry, M.L., Parvizi, J., Hua, L.H., Butts-Pauly, K., Wandell, B.A., 2013. Quantifying the local tissue volume and composition in individual brains with magnetic resonance imaging. Nat. Med. 19, 1667–1672. https://doi.org/10.1038/nm.3390.

Nieuwenhuys, R., Broere, C.A.J., 2017. A map of the human neocortex showing the estimated overall myelin content of the individual architectonic areas based on the studies of Adolf Hopf. Brain Struct. Funct. 222, 465–480. https://doi.org/10.1007/s00429-016-1228-7.

Oishi, H., Takemura, H., Aoki, S.C., Fujita, I., Amano, K., 2018. Microstructural properties of the vertical occipital fasciculus explain the variability in human stereoacuity. Proc. Natl. Acad. Sci. 115, 12289–12294. https://doi.org/10.1101/288753.

Pestilli, F., Yeatman, J.D., Rokem, A., Kay, K.N., Wandell, B. a, 2014. Evaluation and statistical inference for human connectomes. Nat. Methods. https://doi.org/10.1038/nmeth.3098.

Rosenke, M., Weiner, K.S., Barnett, M.A., Zilles, K., Amunts, K., Goebel, R., Grill-Spector, K., 2018. A cross-validated cytoarchitectonic atlas of the human ventral visual stream. Neuroimage 170, 257–270. https://doi.org/10.1016/j.neuroimage.2017.02.040.

Sandip, Panesar, S., Tiago, J., Belo, A., Yeh, F.-C., Fernandez, J.C., Fernandez-Miranda, J.C., 2018. Structure, Asymmetry and Segmentation of the Human Parietal Aslant and Vertical Occipital Fasciculi. https://doi.org/10.1101/252825.

Schleicher, A., Amunts, K., Geyer, S., Kowalski, T., Zilles, K., 1998. An observer-independent cytoarchitectonic mapping of the human cortex using a stereological approach. Acta Stereol.

Schurr, R., Duan, Y., Norcia, A.M., Ogawa, S., Yeatman, J.D., Mezer, A.A., 2018. Tractography optimization using quantitative T1 mapping in the human optic radiation. Neuroimage 181, 645–658. https://doi.org/10.1016/j.neuroimage.2018.06.060.

Smith, R.E., Tournier, J., Calamante, F., Connelly, A., 2012. Anatomically-constrained tractography: improved diffusion MRI streamlines tractography through effective use of anatomical information. Neuroimage 62, 1924–1938. https://doi.org/10.1016/j.neuroimage.2012.06.005.

Smith, S.M., Jenkinson, M., Woolrich, M.W., Beckmann, C.F., Behrens, T.E.J., Johansen-Berg, H., Bannister, P.R., De Luca, M., Drobnjak, I., Flitney, D.E., Niazy, R.K., Saunders, J., Vickers, J., Zhang, Y., De Stefano, N., Brady, J.M., Matthews, P.M., 2004. Advances in functional and structural MR image analysis and implementation as FSL. Neuroimage 23, S208–S219. https://doi.org/10.1016/J.NEUROIMAGE.2004.07.051.

Sotiropoulos, S.N., Moeller, S., Jbabdi, S., Xu, J., Andersson, J.L., Auerbach, E.J., Yacoub, E., Feinberg, D., Setsompop, K., Wald, L.L., Behrens, T.E.J., Ugurbil, K., Lenglet, C., 2013. Effects of image reconstruction on fiber orientation mapping from multichannel diffusion MRI: reducing the noise floor using SENSE. Magn. Reson. Med. 70, 1682–1689. https://doi.org/10.1002/mrm.24623.

Stanisz, G.J., Webb, S., Munro, C.A., Pun, T., Midha, R., 2004. MR properties of excised neural tissue following experimentally induced inflammation. Magn. Reson. Med. 51, 473–479. https://doi.org/10.1002/mrm.20008.

Stikov, N., Perry, L.M., Mezer, A., Rykhlevskaia, E., Wandell, B.a., Pauly, J.M., Dougherty, R.F., 2011. Bound pool fractions complement diffusion measures to describe white matter micro and macrostructure. Neuroimage 54, 1112–1121. https://doi.org/10.1016/j.neuroimage.2010.08.068.

Stüber, C., Morawski, M., Schäfer, A., Labadie, C., Wähnert, M., Leuze, C., Streicher, M., Barapatre, N., Reimann, K., Geyer, S., Spemann, D., Turner, R., 2014. Myelin and iron concentration in the human brain: a quantitative study of MRI contrast. Neuroimage 93 (Pt 1), 95–106. https://doi.org/10.1016/j.neuroimage.2014.02.026.

Takemura, H., Pestilli, F., Weiner, K.S., 2018. Comparative neuroanatomy: integrating classic and modern methods to understand association fibers connecting dorsal and ventral visual cortex. Neurosci. Res. https://doi.org/10.1016/J.NEURES.2018.10.011.

Takemura, H., Pestilli, F., Weiner, K.S., Keliris, A., Landi, M., Sliwa, J., Ye, F.Q., Barnett, M.A., Leopold, D.A., Freiwald, W.A., Logothetis, N.K., Wandell, B.A., 2017. Occipital white matter tracts in human and macaque. Cerebr. Cortex 27, 3346–3359. https://doi.org/10.1093/cercor/bhx070.

Takemura, H., Rokem, A., Winawer, J., Yeatman, J.D., Wandell, B.A., Pestilli, F., 2016. A major human white matter pathway between dorsal and ventral visual cortex. Cerebr. Cortex 26, 2205–2214. https://doi.org/10.1093/cercor/bhv064.

Thiebaut de Schotten, M., ffytche, D.H., Bizzi, A., Dell'Acqua, F., Allin, M., Walshe, M., Murray, R., Williams, S.C., Murphy, D.G.M., Catani, M., 2011. Atlasing location, asymmetry and inter-subject variability of white matter tracts in the human brain with MR diffusion tractography. Neuroimage 54, 49–59. https://doi.org/10.1016/J.NEUROIMAGE.2010.07.055.

Tournier, J.-D., Calamante, F., Connelly, A., 2012. MRtrix: diffusion tractography in crossing fiber regions. Int. J. Imaging Syst. Technol. 22, 53–66. https://doi.org/10.1002/ima.22005.

Wang, L., Mruczek, R.E.B., Arcaro, M.J., Kastner, S., 2015. Probabilistic maps of visual topography in human cortex. Cerebr. Cortex 25, 3911–3931. https://doi.org/10.1093/cercor/bhu277.

Wang, Yibao, Wu, Y., Sun, D., Wang, Yong, Wang, Yunjie, 2016. Tracing short connections of the temporo-parieto-occipital region in the human brain using diffusion spectrum imaging and fiber dissection. Brain Res. 1646, 152–159. https://doi.org/10.1016/j.brainres.2016.05.046.

Wasserthal, J., Neher, P., Maier-Hein, K.H., 2018. TractSeg - fast and accurate white matter tract segmentation. Neuroimage 183, 239–253. https://doi.org/10.1016/J.NEUROIMAGE.2018.07.070.

Weiner, K.S., Barnett, M.A., Lorenz, S., Caspers, J., Stigliani, A., Amunts, K., Zilles, K., Fischl, B., Grill-Spector, K., 2017. The cytoarchitecture of domain-specific regions in human high-level visual cortex. Cerebr. Cortex 27, 146–161. https://doi.org/10.1093/cercor/bhw361.

Weiner, K.S., Golarai, G., Caspers, J., Chuapoco, M.R., Mohlberg, H., Zilles, K., Amunts, K., Grill-Spector, K., 2014. The mid-fusiform sulcus: a landmark identifying both cytoarchitectonic and functional divisions of human ventral temporal cortex. Neuroimage 84, 453–465. https://doi.org/10.1016/j.neuroimage.2013.08.068.

Weiner, K.S., Natu, V.S., Grill-Spector, K., 2018. On object selectivity and the anatomy of the human fusiform gyrus. Neuroimage 173, 604–609. https://doi.org/10.1016/j.neuroimage.2018.02.040.

Weiner, K.S., Yeatman, J.D., Wandell, B.A., 2016. The posterior arcuate fasciculus and the vertical occipital fasciculus. Cortex. https://doi.org/10.1016/j.cortex.2016.03.012.

Wilkinson, M., Lim, A.R., Cohen, A.H., Galaburda, A.M., Takahashi, E., 2017. Detection and growth pattern of arcuate fasciculus from newborn to adult. Front. Neurosci. 11, 389. https://doi.org/10.3389/fnins.2017.00389.

Yeatman, J.D., Dougherty, R.F., Myall, N.J., Wandell, B.A., Feldman, H.M., 2012. Tract profiles of white matter properties: automating fiber-tract quantification. PLoS One 7, e49790. https://doi.org/10.1371/journal.pone.0049790.

Yeatman, J.D., Wandell, B.A., Mezer, A.A., 2014a. Lifespan maturation and degeneration of human brain white matter. Nat. Commun. 5, 4932. https://doi.org/10.1038/ncomms5932.

Yeatman, J.D., Weiner, K.S., Pestilli, F., Rokem, A., Mezer, A., Wandell, B.A., 2014b. The vertical occipital fasciculus: a century of controversy resolved by in vivo measurements. Proc. Natl. Acad. Sci. 111, E5214–E5223. https://doi.org/10.1073/pnas.1418503111.